

Dependence of angular momentum of fission fragments on total kinetic energy in spontaneous fission of ^{252}Cf

A. Rahmatinejad,¹ T. M. Shneidman,^{1,*} G.G. Adamian,¹ and N. V. Antonenko^{1,2}

¹*Joint Institute for Nuclear Research, Dubna, 141980, Russia*

²*Tomsk Polytechnic University, Tomsk, 634050, Russia*

Abstract

A weak dependence of the angular momentum of ^{144}Ba fragments, produced in the spontaneous fission of ^{252}Cf , on the total kinetic energy (TKE) was recently observed [1]. To investigate this phenomenon, we propose a model describing the evolution of the fissioning nucleus toward scission. The model assumes that after tunneling through the fission barrier, the nucleus can be represented by a superposition of dinuclear systems (DNS). We calculate main fission observables, including mass, TKE, and neutron multiplicity distributions, and compare them with experimental data. The angular motion in the DNS is treated quantum-mechanically, yielding the angular momentum distribution of DNS nuclei at scission configurations leading to ^{144}Ba fragments. Within this framework, we successfully reproduce and explain the experimentally observed dependence of the average angular momentum of ^{144}Ba on TKE.

PACS numbers: 25.85.Ca, 27.80.+w, 21.10.Tg, 21.60.Ev, 21.60.-n

Keywords: spontaneous fission, angular momentum of fission fragments, scission point model

*Electronic address: shneyd@theor.jinr.ru

I. INTRODUCTION

Despite the long history of studying spontaneous fission (SF), new experimental data are still emerging, reviving interest in this subject. Although there is a general understanding of key properties of SF process, various theoretical models are based on different assumptions to describe fission observables. New experimental findings not only validate and discriminate these models, but also offer fresh insights helping to refine our understanding of the fission mechanism.

Theoretical models of SF diverge particularly in two aspects. First, they differ in understanding at what elongation of fissioning nucleus the distribution of primary fission fragments is formed. Second, an important question is how the available energy at this elongation is distributed between the excitation and deformation energy of the fragments. Both aspects are crucial for describing the gross properties of SF, such as mass/charge distributions, total kinetic energy (TKE), and neutron multiplicity. However, the splitting between excitation and deformation energies appears particularly decisive in describing correlations between observables, such as the relationship between the average number of neutrons emitted from fission fragments and TKE, or between TKE and fission fragment mass [2].

The experimental data related to the measurement of the angular momenta of fission fragments, have shown that fission fragments possess significant angular momentum, even in the SF of even-even nuclei that occurs from the 0^+ state [3–6]. Mechanisms based on angular motion in scission configurations have been proposed in Refs. [7–18] and successfully applied to describe the average angular momenta of fission fragments. The measurements revealed an absence of correlation between the spins of conjugate fragments [19]. Another interesting observation is related to the strong correlation (saw-tooth behavior) between the average angular momentum of fragments and their mass. These observations provide a good ground for testing existing SF models.

In different models, the absence of correlation between angular momenta of the fission fragments is attributed to the large moment of inertia associated with their relative rotation [17, 18, 20]. However, there are two different approaches to explain the sawtooth behavior of average angular momentum as a function of fragment mass. In Ref. [12], it is assumed that most of the energy available at scission contributes to excitation energy of the fragments while fragments deformations remain close to those of their ground states. In this case, the

sawtooth behavior arises from different structure of excitation spectrum of collective states for conjugate fragments. Conversely, in Refs. [14, 20] most of the energy is stored as the deformation energy of the fragments, with relatively low excitation energy. Here, the sawtooth pattern originates from the fact that the softer fragment possess larger deformation resulting in larger average angular momentum.

Since both approaches describe sawtooth behavior, the question of the balance between excitation and deformation energy at scission might require examining correlations among other observables. Recently, such a correlation was reported in Ref. [1] for the fission fragment ^{144}Ba , where almost an absence of correlation between its angular momentum and TKE was observed. This new data supplemented by the correlation between average number of the emitted neutrons and average TKE [2] gives a possibility to answer this question.

At first glance, in contrast to the experiment, both types of model should lead to an increase of the average angular momenta of the fragments with decreasing TKE. If the fissioning nucleus at scission is hot then angular momentum of the fission fragments is roughly described by the Boltzmann distribution [12]. Therefore, the decrease of TKE and subsequent increase of excitation energy would lead to an increase of angular momentum of fission fragments. If available energy is mainly stored as deformation energy, the decrease of TKE would lead to increase of deformation as shown in Ref. [20], that can also lead to the increase of angular momentum. Therefore, this puzzling behavior of angular momentum vs TKE is a good test for the models. It is important, in addition to the correlations, to describe simultaneously other fission observables within unique approach.

For this purpose we employ the fission model introduced in Ref. [21] supplemented by the description of collective states related to the angular motion of fission fragments at scission [20]. As assumed in this model, after tunneling through the fission barrier the nucleus can be represented by a superposition of two fragments at touching. Variations in deformation and mass asymmetry occur in these systems until dinuclear systems (DNS) decay. The characteristics of DNS fragments, including their deformations, mass asymmetry, and energy, play a decisive role in shaping the observable distributions associated with fission. The proposed approach is a modification of the scission point model which takes into account that not all scission configurations are dynamically equally achievable. It can be thought of as a model of random walk among various scission configurations. Recent microscopic calculations in the framework of time-dependent density functional theory support the scission point model

[22].

The paper is organized as follows. In Sec. II, we present the model used to describe the SF process as an evolution of initially formed DNS configurations toward scission. The basic assumptions of the model and the main characteristics defining different DNS configurations—including potential energies, excitation energy, and level densities—are detailed in Sec. II A. Section II B introduces the method for calculating the primary fission fragment distribution. Section II C provides a quantum-mechanical treatment of collective angular motion in the DNS. Finally, Sec. II D presents the expressions used to derive various primary fission fragment distributions, such as mass, TKE, neutron multiplicity, and average angular momentum. The calculated fission observables for the SF of ^{252}Cf are presented in Sec. III A. In Sec. III B, we identify the DNS configurations leading to the formation of the post-scission fragment ^{144}Ba and in Sec. III C we analyze angular vibrations in the selected DNS. Section III D presents the calculated average angular momenta of primary fission fragments as a function of TKE. Finally, Sec. III E discusses the average angular momentum of post-scission ^{144}Ba fragments as a function of TKE. The conclusions are summarized in Sec. IV.

II. MODEL

A. Fissioning nucleus at scission

After crossing the fission barrier, the fissioning nucleus AZ is treated as a superposition of various DNS. As a DNS we understand a system of two fragments ($i = 1, 2$) in touching configuration characterized by their charges ($Z_{1,2}$) and masses ($A_{1,2}$), where $Z_1 + Z_2 = Z$ and $A_1 + A_2 = A$. The shape of each fragment is modeled as an axially-symmetric ellipsoid with major-to-minor axes ratio denoted as $b_{1,2}$. The quantities $b_{1,2}$ are related to the conventional quadrupole deformation parameters $\beta_{1,2}$ by equating the quadrupole moments calculated for ellipsoidal and spheroidal shapes:

$$\begin{aligned} Q(\beta_{1,2}) &= Q(b_{1,2}), \\ b_{1,2} &\approx \frac{1 + \sqrt{5/4\pi}\beta_{1,2}}{1 - \sqrt{5/16\pi}\beta_{1,2}}. \end{aligned} \tag{1}$$

In the following, each DNS is characterized by a set $(Z_i, A_i, \beta_i, i = 1, 2)$.

Due to the competition between attractive nuclear and repulsive Coulomb parts of nucleus-nucleus interaction, the potential energy of DNS as a function of relative distance coordinate R has a pocket or at least is flat in the vicinity of touching configuration at $R = R_m(\beta_1, \beta_2)$. Therefore, the DNS does not decay instantly. Instead, the decay of DNS competes with an evolution in mass/charge asymmetry coordinates and in deformation of the fragments.

The shapes of the DNS nuclei, their masses, charges, and the distribution of angular momenta, as well as the excitation energy of DNS at the moment of decay determine the primary fission fragment distributions.

For each DNS one can calculate the potential energy $U(Z_{1,2}, A_{1,2}, \beta_{1,2})$ and excitation energy $E^*(Z_{1,2}, A_{1,2}, \beta_{1,2})$. The potential energy of DNS consists of terms describing energies of the constituent fragments ($U_i^{LD} + \delta E_i^{sh}$) and the energy of their interaction V_{int} [23]:

$$\begin{aligned} U(Z_{1,2}, A_{1,2}, \beta_{1,2}) = & U_1^{LD}(Z_1, A_1, \beta_1) + \delta E_1^{sh}(Z_1, A_1, \beta_1) \\ & + U_2^{LD}(Z_2, A_2, \beta_2) + \delta E_2^{sh}(Z_2, A_2, \beta_2) \\ & + V_{int}(Z_{1,2}, A_{1,2}, \beta_{1,2}, R_m(\beta_1, \beta_2)). \end{aligned} \quad (2)$$

The energy of the i -th fragment consists of the liquid-drop part U_i^{LD} and shell correction δE_i^{sh} . The liquid-drop energies are calculated within the prescription given in Ref. [24]. Shell corrections are acquired using Strutinsky approach with the single-particle spectra of deformed Nilsson-like Hamiltonian [25]. The parameters of spin-orbit interaction are taken as in Ref. [26, 27].

The interaction potential V_{int} in Eq. (2) is calculated for the pole-to-pole touching configuration of the fragments. The details of calculations are presented in Refs. [20, 23]. It is assumed that energies of zero-point vibrations in relative distance and in the orientation of fragments are taken into account by the choice of effective interaction. The orientation dependence of DNS potential energy is excluded from V_{int} . The collective angular motion of the fragments is treated as an intrinsic excitations of DNS, therefore this dependence contributes to the energies of collective angular motion in DNS (see Sec.II C).

An important ingredient needed to characterize a DNS is the excitation energy. Denoting the energy of the fissioning nucleus as $U_0(Z, A)$, the excitation energy is given as

$$\begin{aligned} E^*(Z_{1,2}, A_{1,2}, \beta_{1,2}) = & U_0(Z, A) - U(Z_{1,2}, A_{1,2}, \beta_{1,2}), \\ U_0(Z, A) = & U^{LD}(Z, A, \beta^{(gs)}) + \delta E^{sh}(Z, A, \beta^{(gs)}), \end{aligned} \quad (3)$$

where the ground-state deformations $\beta^{(gs)}$ of the ^{252}Cf are taken from [28].

The intrinsic state of the DNS is characterized by its level density $\rho(E^*, DNS)$, which consists of intrinsic level density and the level density of collective states associated with the angular motions in DNS. The intrinsic level density of DNS is calculated as a folding of the level densities $\rho_{1,2}$ of its constituent fragments [29]

$$\rho_{int}(E^*, DNS) = \int \rho_1(\varepsilon) \rho_2(E^* - \varepsilon) d\varepsilon. \quad (4)$$

To obtain the level densities of DNS fragments, the superfluid formalism is used [30–32]. The required single-particle spectra are calculated by diagonalization of the Nilsson Hamiltonian for given mass, charge, and deformation of the fragment. This approach allows us to take into account not only the excitation energy but also the deformation dependence of the level densities [33–36].

The integrant in Eq. (4) is strongly peaked function of ε , so the excitation energies of DNS fragments E_1^* and $E_2^* = E^* - E_1^*$ can be obtained from the condition

$$\left(\frac{1}{\rho_1(\varepsilon)} \frac{d\rho_1(\varepsilon)}{d\varepsilon} \right) \Big|_{\varepsilon=E_1^*} = \left(\frac{1}{\rho_2(\varepsilon)} \frac{d\rho_2(\varepsilon)}{d\varepsilon} \right) \Big|_{\varepsilon=E_2^*} = T^{-1}. \quad (5)$$

This expression can be used to define the temperature T of the DNS. Although temperature is not explicitly present in the calculations, its value is useful for qualitatively assessing the rigidity of the DNS with respect to the excitation of various degrees of freedom.

In the calculation of $\rho_{1,2}$, the collective enhancement factors are not taken into account. The reason is that being constituents of DNS the collective motion of fragments are not independent of each other. Therefore, instead of collective enhancements of individual DNS fragments we take into account the collective excited states of DNS. Moreover, since the dynamics of DNS in fragments deformation and in relative distance are treated explicitly, the associated collective states are not incorporated to the DNS level densities. Therefore, the only collective states which contribute to the level densities are related to angular motion in DNS as discussed in Sec. II C.

Denoting the energies of these collective states as E_x^* , ($x = 0, 1, 2, \dots$), the DNS level density is obtained as a folding of intrinsic level density and the density of collective states as [33, 37]

$$\rho(E^*, DNS) = \sum_x \rho_{int}(E^* - E_x^*, DNS). \quad (6)$$

Note that if the excitation energy E^* for a given DNS configuration is small, then among the excitations of angular motions only a few contributes to $\rho(E^*, DNS)$.

B. Distribution of primary fission fragments

The evolution of DNS distribution in time is described using the master equation. The space of deformations and masses of the fragments is discretized with grid sizes $\Delta\beta_i = 0.05$, and $\Delta A_i = \Delta Z_i = 1$ or $\Delta A_i = \Delta N_i = 1$, respectively. Each of the obtained cells is characterized by the index

$$n = (Z_i, A_i, \beta_i, i = 1, 2). \quad (7)$$

Defining the probability for the DNS to be in cell n as $P(n)$, the time dependence of this probability is governed by the master equation [38]:

$$\frac{d}{dt}P(n, t) = \sum_{n'} [\Lambda(n'|n)P(n', t) - \Lambda(n|n')P(n, t)] - \Lambda_{decay}(n)P(n, t), \quad (8)$$

with the initial condition $P_0(n) = P(n, t = 0)$ determined by the superposition of the initially formed DNS. In Eq. (8), $\Lambda(n'|n)$ and $\Lambda(n|n')$ represent the rates of transitions from n' to n and vice versa. The DNS decay rate is denoted as Λ_{decay} . Evolution is assumed to occur only between neighboring cells. The distribution of primary fission fragments $P_f(n[Z_1, A_1, \beta_1, Z_2, A_2, \beta_2])$ is obtained by solving Eq.(8) with Monte-Carlo technique.

The transition rates in Eq. (8) are expressed in terms of microscopic transition probabilities $\lambda_{nn'}$ and the level densities of the final states [38, 39]:

$$\begin{aligned} \Lambda(n|n') &= \lambda_{nn'}\rho(E_{n'}^*, n'), \\ \Lambda(n'|n) &= \lambda_{n'n}\rho(E_n^*, n), \\ \lambda_{n'n} &= \lambda_{nn'}. \end{aligned} \quad (9)$$

Microscopic transition probabilities are defined up to a constant parameter as [38]

$$\lambda_{n'n} = \lambda_{nn'} = \lambda^{(j)} / \sqrt{\rho(E_{n'}^*, n')\rho(E_n^*, n)}, \quad j = (A, b). \quad (10)$$

Here, $\lambda^{(A)}$ is used when n and n' differ by the fragment masses (nucleon transfer between the fragments), and $\lambda^{(b)}$ is used when n and n' differ by fragment deformations. In this study,

$\lambda^{(A,b)}$ are treated as the parameters of the model and adjusted based on analysis of average neutron multiplicities in even-even $^{242-248}\text{Cm}$ and $^{246-254}\text{Cf}$ nuclei.

The decay probability in Eq. (8) is treated as

$$\Lambda_{decay}(n) = \lambda^d \rho_{s.p.}(E_n^* - V_B^n, n), \quad (11)$$

where microscopic decay probability is

$$\lambda^d = \begin{cases} 1/\rho(E_n^*, n), & \text{if } (E_n^* > V_B^n), \\ 0, & \text{if } (E_n^* < V_B^n). \end{cases} \quad (12)$$

In Eq. (11), $\rho_{s.p.}(E_n^* - V_B^n, n)$ is the level density at the top of barrier in R keeping the DNS. In Eq. (12), tunneling through the potential barrier is disregarded. If excitation energy E_n^* of DNS is less than the barrier height V_B^n , the decay channel is closed. If there is no barrier in the potential energy, then $\rho_{s.p.}(E_n^*, n)$ is calculated at touching configuration ($V_B^n = 0$).

To choose the initial distribution $P_0(n, t = 0)$ we select the DNS whose quadrupole moment Q_n is within 10% range around the quadrupole moment Q_{in} of an ellipsoid with an axes ratio b_{in} :

$$|Q_n - Q_{in}| \leq 0.1 Q_{in}. \quad (13)$$

The value b_{in} is treated as a parameter of the model.

Its choice is governed by two conditions. First, the value of b_{in} must correspond to the elongations of the fissioning nucleus that exceed the position of the fission barrier. Secondly, at this point it should be possible to present the fissile nucleus as a superposition of binary systems (DNS). As follows from the observation that hyperdeformed states of nuclei ($b = 3 : 1$) can be treated as DNS [40–43], both these conditions can be fulfilled for $b_{in} > 3.0$. It is interesting that our calculations also show that the DNS which can potentially contribute to the initial state ($E_n^* > 0$) starts to emerge in this region. The chosen DNS are then distributed proportionally to their level densities:

$$\frac{P_0(n)}{P_0(n')} = \frac{\rho(E_n^*, n)}{\rho(E_{n'}^*, n')}. \quad (14)$$

C. Angular motions of fission fragments at scission

In the model presented, it is assumed that fragments acquire angular momentum at scission due to the collective angular motion in DNS. Moreover, as discussed above, these

states contribute to the collective enhancement of DNS level densities (see Eq. (6)). The detailed quantum-mechanical description of this collective mode is presented in Ref. [20] to describe an absence of correlation between average angular momenta of fission fragments and the sawtooth behavior of average angular momentum versus mass of fragments. Here, we present a brief description of the main aspects of the model.

The schematic representation of DNS ($Z_{1,2}, A_{1,2}, \beta_{1,2}$) is shown in Fig. 1. The center of laboratory system $Oxyz$ is placed in the center of mass of DNS. The vector of relative distance between the centers of masses of the fragments is denoted as $\mathbf{R} = (R, \theta_0, \phi_0)$, where $\Omega_0 = (\theta_0, \phi_0)$ are the angles determining the orientation of \mathbf{R} with respect to the laboratory system. The body-fixed (molecular) coordinate system $Ox_0y_0z_0$ is taken in such a way that the direction of Oz_0 axis coincides with vector \mathbf{R} . The centers of the intrinsic coordinate system of the i -th fragment O_i are placed in the centers of mass of the corresponding fragment. The orientation of intrinsic coordinate systems $O_ix_iy_iz_i$ of i -th fragment with respect to the laboratory system is defined by the angles $\Omega_i = (\phi_i, \theta_i, 0)$. Since the fragments are assumed to be axially-symmetric, only two Euler angles are required. The orientations of the fragments and of \mathbf{R} with respect to the laboratory system are not restricted. We assume that before decay, fragments at any orientation stay in touching configuration defined by $R_m(\Omega_0, \Omega_1, \Omega_2)$. Although the distance R_m between the fragments for a given orientation does not depend on the rotation of the system as a whole, it still depends on angles (θ_0, ϕ_0) , because all angles are defined with respect to the laboratory frame rather than to the body-fixed frame.

The collective motion in DNS is related to the rotation of the fragments and to the relative rotation of DNS as a whole with respect to the laboratory system. The kinetic energy is then written as

$$T = \frac{\hbar^2 \hat{I}_0^2}{2\mu R^2} + \frac{\hbar^2 \hat{I}_1^2}{2\mathfrak{I}_1} + \frac{\hbar^2 \hat{I}_2^2}{2\mathfrak{I}_2}, \quad (15)$$

where angular momentum operators are given as

$$\hat{I}_i^2 = - \left(\frac{1}{\sin \theta_i} \frac{\partial}{\partial \theta_i} \sin \theta_i \frac{\partial}{\partial \theta_i} + \frac{1}{\sin^2 \theta_i} \frac{\partial^2}{\partial \phi_i^2} \right), \quad (i = 0, 1, 2). \quad (16)$$

In Eq. (15), $\mathfrak{I}_{1,2}$, and $\mathfrak{I}_R = \mu R^2$ are the moments of inertia of the fragments and DNS as a whole, respectively, $\mu = m_0 A_1 A_2 / A$ is the reduced mass, and m_0 is the nucleon mass. The

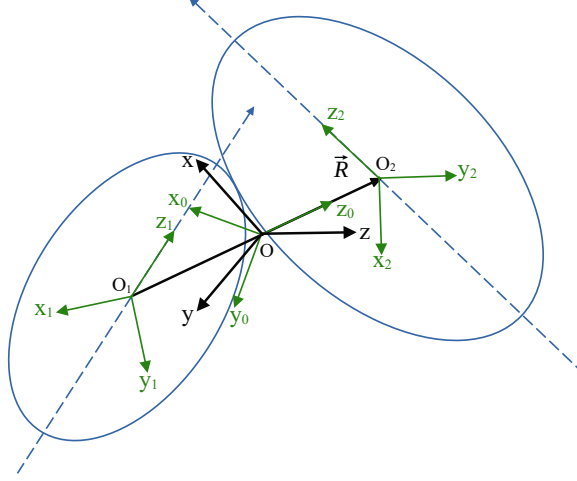


FIG. 1: Schematic presentation of DNS or scission configuration of fissioning nucleus. The laboratory coordinate system $Oxyz$, as well as molecular $Ox_0y_0z_0$ and intrinsic coordinate systems $O_ix_iy_iz_i$, ($i = 1, 2$) of the fragments are marked. Center of laboratory and molecular coordinate systems O coincide with the center of mass of DNS. Centers of intrinsic systems $O_{1,2}$ coincide with the center of mass of the corresponding fragments. The vector of distance between the centers of mass of the fragments is denoted as \mathbf{R} .

moments of inertia of the fragments are taken in the rigid body limit as

$$\begin{aligned} \mathfrak{I}_i &= \int d\tau (x_i^2 + z_i^2) \rho_i(\mathbf{r}) = \int d\tau (y_i^2 + z_i^2) \rho_i(\mathbf{r}) \\ &\approx \frac{2}{5} m_0 A_i R_i^2 \left(1 + \sqrt{\frac{5}{16\pi}} \beta_i + \frac{20}{7\pi} \beta_i^2 + \frac{5\sqrt{5}}{8\pi^{3/2}} \beta_i^3 + \dots \right). \end{aligned} \quad (17)$$

The integrations in Eq. (17) are performed in the intrinsic coordinate system $O_ix_iy_iz_i$ of the corresponding fragments. The second line of Eq. (17) is obtained under the assumption that the nuclear densities ρ_i ($i = 1, 2$) of the fragments in their respective intrinsic coordinate systems are constant in the volume defined by the surface $R_i(\theta, \phi) = R_{0i}(1 + \beta_i Y_{20}(\theta, \phi))$. Here, $R_{0i} = r_0 A_i^{1/3}$ with $r_0 = 1.2$ fm. The assumption of the rigid body moment of inertia stems from the fact that even at low excitation energies, the nucleus transits from a superfluid to a normal phase. This transition is known to result in an increase of the moment of inertia towards the rigid body limit. Thus, the use of rigid body moments of inertia is a realistic approximation.

The potential energy is calculated as a sum of nuclear V_N , and Coulomb interactions V_C :

$$V_{int}(\Omega_i) = V_C(R_m(\Omega_i), \Omega_i) + V_N(R_m(\Omega_i), \Omega_i), \quad (i = 0, 1, 2) \quad (18)$$

at touching configuration $R = R_m(\Omega_0, \Omega_1, \Omega_2)$. For a given distance R between the fragments and the orientation defined by angles $\Omega_{i=0,1,2}$, the Coulomb interaction is calculated as a multipole expansion

$$V_C(R, \Omega_i) = \sum_{\lambda_1 \lambda_2} V_{\lambda_1, \lambda_2}(\beta_1, \beta_2) \left[[Y_{\lambda_1}(\Omega_1) \times Y_{\lambda_2}(\Omega_2)]_{(\lambda_1 + \lambda_2)} \times Y_{\lambda_1 + \lambda_2}(\Omega_0) \right]_{(0,0)},$$

$$V_{\lambda_1, \lambda_2}(\beta_1, \beta_2) = (-1)^{\lambda_2} \sqrt{\frac{(4\pi)^3 (2\lambda_1 + 2\lambda_2)!}{(2\lambda_1 + 1)!(2\lambda_2 + 1)!}} \frac{Q_{\lambda_1}^{(1)}(\beta_1) Q_{\lambda_2}^{(2)}(\beta_2)}{R^{\lambda_1 + \lambda_2 + 1}}, \quad (19)$$

where multipole moments of the fragments are

$$Q_{\lambda}^{(i)}(\beta_i) = \sqrt{\frac{4\pi}{2\lambda + 1}} \int \rho_i(\mathbf{r}_i) r_i^{\lambda} Y_{\lambda 0}(\theta, \phi) d\mathbf{r}_i. \quad (20)$$

The nuclear part of interaction is calculated using the double-folding procedure [23] with density-dependent effective nucleon–nucleon interaction [44]. The nuclear densities ρ_i are approximated by Fermi distributions with the radius parameter $r_0 = 1.15$ fm. The diffuseness parameters are taken as $a = 0.56 \sqrt{B_n^{(0)}/B_n}$, where $B_n^{(0)}$ and B_n are the neutron binding energies of the nucleus under study and the heaviest isotope of the same element, respectively. Details of the calculations are presented in Refs. [23, 45].

Calculating potential energy at touching configuration for all orientations, we expand it in a basis of tripolar spherical functions

$$V_{int}(\Omega_{i=0,1,2}) = \sum_{\lambda_0, \lambda_1, \lambda_2} C_{\lambda_0, \lambda_1, \lambda_2}(\beta_1, \beta_2) \left[[Y_{\lambda_1}(\Omega_1) \times Y_{\lambda_2}(\Omega_2)]_{\lambda_0} \times Y_{\lambda_0}(\Omega_0) \right]_{(0,0)}, \quad (21)$$

where the stiffness parameters $C_{\lambda_0, \lambda_1, \lambda_2}$ are obtained by fitting the calculated potential energy. The tripolar spherical functions are defined as [46]

$$\begin{aligned} & \left[[Y_{\lambda_1}(\Omega_1) \times Y_{\lambda_2}(\Omega_2)]_{\lambda_{12}} \times Y_{\lambda_0}(\Omega_0) \right]_{(\lambda\mu)} \equiv [[\lambda_1 \times \lambda_2]_{\lambda_{12}} \times \lambda_0]_{(\lambda\mu)} \\ & = \sum_{\mu_0, \mu_1, \mu_2, \mu_{12}} C_{\lambda_1 \mu_1, \lambda_2 \mu_2}^{\lambda_{12} \mu_{12}} C_{\lambda_{12} \mu_{12}, \lambda_0 \mu_0}^{\lambda \mu} Y_{\lambda_1 \mu_1}(\Omega_1) Y_{\lambda_2 \mu_2}(\Omega_2) Y_{\lambda_0 \mu_0}(\Omega_0). \end{aligned} \quad (22)$$

The Hamiltonian for the angular motion in DNS is then written as

$$H = \hat{T} + V_{int}(\Omega_{i=0,1,2}) - V_{int}(\Omega_{i=0,1,2} = 0), \quad (23)$$

$$\hat{T} = \frac{\hbar^2 \hat{I}_0^2}{2\mu R^2} + \frac{\hbar^2 \hat{I}_1^2}{2\mathfrak{I}_1} + \frac{\hbar^2 \hat{I}_2^2}{2\mathfrak{I}_2}, \quad (24)$$

$$V_{int}(\Omega_{i=0,1,2}) = \sum_{\lambda_0, \lambda_1, \lambda_2} C_{\lambda_0, \lambda_1, \lambda_2} \left[[\lambda_1 \times \lambda_2]_{\lambda_0} \times \lambda_0 \right]_{(0,0)}. \quad (25)$$

In the Hamiltonian (23), the energy of pole-to-pole touching configuration is extracted from the DNS potential energy. The energy of pole-to-pole configuration is taken into account in Eq. (2). Therefore, the Hamiltonian (23) only takes into account the orientation dependence of DNS potential energy.

For a state with angular momentum I , the Hamiltonian (23) is diagonalized using a set of tripolar spherical functions $[i_0 \times [i_1 \times i_2]_{i_{12}}]_{(I,M)}$. For spontaneous fission of ^{252}Cf , we are interested only in the states $I^\pi = 0^+$. Therefore, the basis set is reduced and the eigenfunctions of 0^+ states of the angular motion are given as

$$\Psi_x = \sum_{i_0 i_1 i_2} a_{i_0 i_1 i_2}^{(x)} [i_0 \times [i_1 \times i_2]_{i_0}]_{(00)}, \quad (x = 0, 1, 2), \quad (26)$$

where $a_{i_0 i_1 i_2}^{(x)}$ are the probability amplitudes obtained by the numerical diagonalization of the Hamiltonian (23). The expression

$$\mathcal{P}(x, i_0 i_1 i_2) = |a_{i_0 i_1 i_2}^{(x)}|^2, \quad (27)$$

defines the probability that the angular momentum of the first fragment, of the second fragment and of DNS as a whole are i_1 , i_2 , and i_0 , respectively. Then the average angular momentum of the fragments and the binary system at the state x is as follows

$$\langle i_j^{(x)} \rangle = \left[\sum_{i_0 i_1 i_2} i_j(i_j + 1) \mathcal{P}(x, i_0 i_1 i_2) \right]^{1/2}, \quad (j = 0, 1, 2). \quad (28)$$

For the DNS characterized by excitation energy E^* , the angular momenta of the fragments are obtained by averaging $\langle i_j^{(x)} \rangle$ over different states x :

$$\langle i_j \rangle = \mathcal{N} \sum_x \langle i_j^{(x)} \rangle \rho_{int}(E^* - E_x, DNS), \quad (j = 0, 1, 2). \quad (29)$$

where $\mathcal{N}^{-1} = \sum_x \rho_{int}(E^* - E_x, DNS)$ is the normalization constant.

D. Distribution of fission observables

Solving Eq. (8), we obtain the distribution of primary fission fragments $P_f(n[Z_1, A_1, \beta_1, Z_2, A_2, \beta_2])$. The mass $Y(A)$ and charge $Y(Z)$ distributions are then calculated by summing over the probabilities of decay from the cells characterized by given mass A or charge Z values of one of the fragments, respectively:

$$\begin{aligned}
Y(A) &= \sum_{n_j} P_f(n_j) [\delta_{A_1,A} + \delta_{A_2,A}], \\
Y(Z) &= \sum_{n_j} P_f(n_j) [\delta_{Z_1,Z} + \delta_{Z_2,Z}].
\end{aligned} \tag{30}$$

For a DNS characterized by index n , the TKE of primary fission fragments is defined as the interaction energy at the top of the barrier $R = R_b$:

$$TKE_n = V_C(n[Z_{1,2}, A_{1,2}, \beta_{1,2}, R_b]) + V_N(n[Z_{1,2}, A_{1,2}, \beta_{1,2}, R_b]). \tag{31}$$

Then the TKE distribution is calculated by summing over the probabilities $P_f(n)$ corresponding to the states with TKE within a given interval 2Δ :

$$Y(TKE) = \sum_j P_f(n_j) \Theta(|TKE_{n_j} - TKE| \leq \Delta), \tag{32}$$

where function $\Theta = 1$ if the condition $|TKE_{n_j} - TKE| \leq \Delta$ is fulfilled and $\Theta = 0$ otherwise.

To obtain the number of neutrons emitted by the fission fragments, we calculate their post-scission excitation energies. These energies originate from two sources: first, the excitation energies $E_{1,2}^*$ which fragments possess at scission (see Eq. (5)); second, energies $E_{1,2}^{def}$ acquired by the fragments after scission due to the relaxation of their shapes back to the ground-state:

$$\begin{aligned}
E_i^{def}(n) &= [U_i^{LD}(Z_i, A_i, \beta_i) + \delta E_i^{sh}(Z_i, A_i, \beta_i)] \\
&\quad - [U_i^{LD}(Z_i, A_i, \beta_i^{gs}) + \delta E_i^{sh}(Z_i, A_i, \beta_i^{gs})], \quad (i = 1, 2).
\end{aligned} \tag{33}$$

The probability $F_{1,2}(x, E_{1,2})$ that a fragment with a given excitation energy $E_{1,2} = E_{1,2}^* + E_{1,2}^{def}$ emits exactly x neutrons is determined through the Monte-Carlo simulation applying probability densities derived from microscopic level densities and using experimental neutron separation energies (see Ref. [47] for details). The probability to emit ν neutrons in a fission event (neutron multiplicity distribution) is then given by the expression:

$$Y(\nu) = \sum_j \left[\sum_{x=1}^{\nu} F_1(x, E_1^{def}(n_j) + E_1^*(n_j)) F_2(\nu - x, E_2^{def}(n_j) + E_2^*(n_j)) \right] P_f(n_j). \tag{34}$$

Using the obtained yields $P_f(n)$, we calculate the angular momentum of a particular primary fission fragment as follows. For a given DNS indexed by n , the average angular

momenta of first $\langle I_1(n) \rangle$ and second $\langle I_2(n) \rangle$ fragments and of the DNS as a whole $\langle I_0(n) \rangle$ are calculated using Eqs. (28), and (29).

Then the average angular momentum of the given primary fission fragment (Z, A) is calculated as:

$$\langle I_{Z,A} \rangle = N \sum_{n_j} P_f(n_j) [\langle I_1(n_j) \rangle \delta_{Z_1,Z} \delta_{A_1,A} + \langle I_2(n_j) \rangle \delta_{Z_2,Z} \delta_{A_2,A}], \quad (35)$$

where $N^{-1} = \sum_{n_j} P_f(n_j) [\delta_{Z_1,Z} \delta_{A_1,A} + \delta_{Z_2,Z} \delta_{A_2,A}]$ is the normalization constant.

If any additional restrictions on the choice of primary fragments, such as, for example, fixed deformation or TKE are imposed, they can be incorporated through additional constraints on the choice of n in Eq. (35). In order to link pre-scission and post-scission distributions one should additionally take into account the change of the fragment mass due to the neutron emission and the angular momentum carried away by neutrons. Following the discussion in [1], we assume that each neutron carries away $\hbar/2$ units of angular momentum.

III. RESULTS

The main goal of this study is to investigate recently observed dependence of angular momentum of ^{144}Ba produced in spontaneous fission of ^{252}Cf on the TKE [1]. For consistency, other fission observables are calculated as well.

A. Mass, TKE, and neutron multiplicity distributions

We first calculate mass, TKE and neutron multiplicity distributions. The results, together with the available experimental data, are shown in Figs. 2(a-c). The average $\langle TKE \rangle$, the width $\langle A_H \rangle$ and light $\langle A_L \rangle$ fragments, and average neutron multiplicity $\langle \nu \rangle$ are listed in Table I. In these calculations we use the following set of parameters: $\lambda^A = 0.18\text{s}^{-1}$, $\lambda^b = 0.2\text{s}^{-1}$, $b_0 = 3.55$. Unlike in the model presented in Ref. [21], here the steps in mass and charge are taken as $\Delta A_i = \Delta Z_i = 1$ or $\Delta A_i = \Delta N_i = 1$. This was done in order to take into account the contribution from DNS with odd-mass fragments. The results are in satisfactory agreement with the experimental data.

For mass distribution, symmetric fission is more pronounced comparing to the experimental data. This is also reflected in that the average heavy fragment mass is overestimated

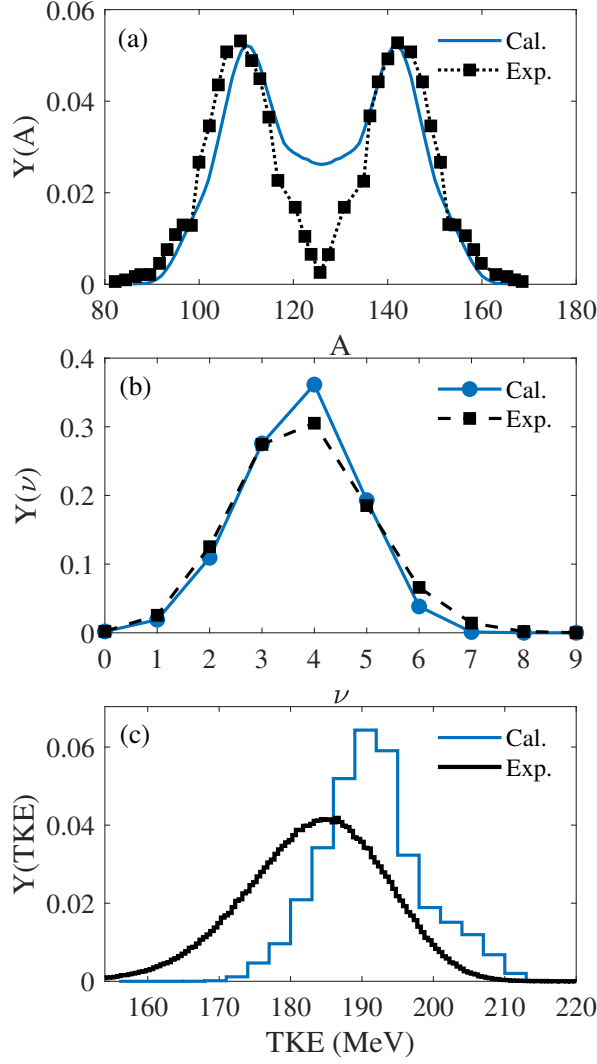


FIG. 2: Calculated (solid lines) and experimental (dashed lines) mass (a), neutron multiplicity (b), and total kinetic energy (c) distributions for spontaneous fission of ^{252}Cf . The experimental data for mass is taken from [52], for neutron multiplicity from [53], and for TKE from [1].

by 3-5 units compared to the experimental data (see Table. I). However, in the region of Ba+Mo mass split (which is of main importance for the present study) our calculations are in a good agreement with the experimental mass distribution.

Since, the average neutron multiplicities are used to define the parameters of the model, the neutron multiplicity distribution is reproduced with a good accuracy (see Fig. 2 (b)). The width of this distribution is also well reproduced. Previously, the model was successfully applied to the description of recent results on neutron multiplicities in transfermium nuclei

TABLE I: The calculated and experimental average $\langle TKE \rangle$, the width of TKE distribution σ_{TKE} , average masses of heavy $\langle A_H \rangle$ and light $\langle A_L \rangle$ fragments together with the average neutron multiplicity $\langle \nu \rangle$.

Quantities	Exp.	Cal.
$\langle TKE \rangle$ (MeV)	189 ± 1 [51] 186.8 [52]	189.93
σ_{TKE} (MeV)	9.43 [51] 11.17 [52]	7.36
$\langle A_H \rangle$	145.7 ± 0.1 [51] 143.4 [52]	140.41
$\langle A_L \rangle$	106.3 ± 0.1 [51] 108.6 [52]	111.59
$\langle \nu \rangle$	3.757 ± 0.01 [53] 3.756 ± 0.031 [54]	3.713

[48–50].

The TKE distribution $Y(TKE)$ is presented in Fig. 2 (c) together with experimental data from Ref. [1]. It is seen that the maximum of calculated distribution is shifted about 5 MeV towards larger TKE and the distribution is narrower to the direction of small TKE.

It is interesting that our $\langle TKE \rangle$ aligns with the average TKE which is given for the first mode in Ref. [51] (see Table. I). In this experiment, two modes were detected for the TKE and neutron emission. Within the configuration space considered, we do not observe the second mode which corresponds to a large number of neutrons. Since our aim is to analyze the angular momentum versus TKE in the range of 170-200 MeV, an absence of second mode does not affect our analysis.

B. Scission DNS configurations leading to ^{144}Ba fission fragment

In order to investigate angular momentum of ^{144}Ba as a function of TKE, we should first determine which DNS configurations lead to the post-scission ^{144}Ba fragment. The proton emission is strongly hindered, therefore, we restrict the consideration by Ba+Mo

scission configurations only. For example, post-scission ^{144}Ba can be obtained from the DNS: $^{144}\text{Ba} + ^{108}\text{Mo}$ at scission under constraint that no neutrons were emitted from Ba after decay.

The post-scission ^{144}Ba is also produced from the following scission configurations:

$$\begin{aligned}
^{144}\text{Ba} + ^{108}\text{Mo} : \quad n_{\text{Ba}} < 1, \\
^{145}\text{Ba} + ^{107}\text{Mo} : \quad 1 \leq n_{\text{Ba}} < 2, \\
^{146}\text{Ba} + ^{106}\text{Mo} : \quad 2 \leq n_{\text{Ba}} < 3, \\
^{147}\text{Ba} + ^{105}\text{Mo} : \quad 3 \leq n_{\text{Ba}} < 4,
\end{aligned} \tag{36}$$

where n_{Ba} is the average number of neutrons emitted from Ba fragment. Other scission configurations leading to post-scission ^{144}Ba are populated with quite small probabilities and are not taken into account.

The probabilities that ^{252}Cf decays from the scission configurations (36) are presented in Fig. 3 as a function of the deformations β_{Mo} and β_{Ba} of the Mo and Ba fragments, respectively. Since the amount of neutrons emitted from Ba is constrained, the decay occurs from the region limited in β_{Ba} . Indeed, following the discussion regarding Eq. (34), the excitation energy required for neutron emission comes from the excitation energy at scission and deformation energy. These energies increase with deformation of fragments. Therefore, restriction on the number of neutrons emitted imposes the restriction on the deformation of Ba at scission configuration.

The number of neutrons emitted from Mo is not constrained. That is why the decay can occur in a wider range of β_{Mo} .

The decay of DNS with given deformations leads to fission event with TKE which is calculated with Eq. (31). The TKE distributions $Y(\text{TKE})$ for the DNS configurations presented in Eq. (36) are shown in Fig. 4. The TKE range is divided into bins with a width of 3 MeV. The $Y(\text{TKE})$ is calculated by summing up the decay probabilities leading to the TKE values within the range ± 1.5 MeV. Each TKE distribution presented in Fig. 4 is normalized to unity for better visibility. As seen from the figure, each DNS has a TKE distribution which is dominant in a certain energy interval. In some cases these intervals overlap with each other. Then, several DNS contribute to the distribution of fission observables at a given TKE simultaneously. The contribution of these systems is determined by their relative decay probabilities.

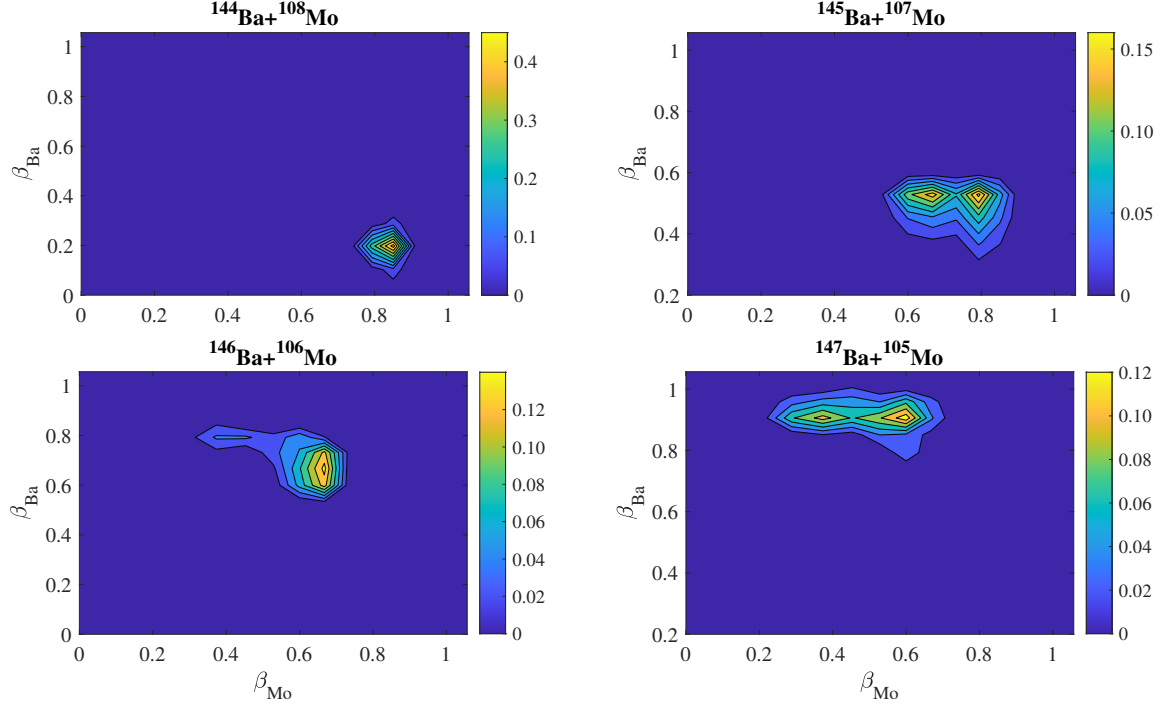


FIG. 3: The decay probabilities of various scission configurations leading to post-scission fragment ^{144}Ba as a function of the deformations β_{Mo} and β_{Ba} of the Mo and Ba fragments, respectively.

C. Description of angular vibrations in scission DNS configurations

For a given TKE bin, the deformations of the DNS fragments change only slightly. Therefore, in the calculation of angular momenta of fission fragments, the deformations of the DNS constituents are averaged inside each bin. The average deformations for each TKE bin together with the corresponding TKE values, decay probabilities and temperatures at scission point for the chosen DNS are listed in Table. II. For these systems we calculate the potential energy for angular vibrations using Eqs. (18), and (21). Diagonalizing the Hamiltonian in Eqs. (23-25), we obtain the spectra of collective 0^+ -states corresponding to angular motions in DNS. For each state x , we calculate the average angular momenta $\langle I_{\text{Mo}}^{(x)} \rangle$, $\langle I_{\text{Ba}}^{(x)} \rangle$, and $\langle I_0^{(x)} \rangle$. Finally, we average over different collective states using Eq. (29). The obtained values of $\langle I_{\text{Mo}} \rangle$, $\langle I_{\text{Ba}} \rangle$, and $\langle I_0 \rangle$ are also presented in Table. II.

As an example, the spectrum of DNS: $^{107}\text{Mo}(\beta_{\text{Mo}} = 0.79) + ^{145}\text{Ba}(\beta_{\text{Ba}} = 0.51)$ is displayed in Fig. 5. To the right side of each excited level x , average angular momenta $\langle I_{\text{Mo}}^{(x)} \rangle$, $\langle I_{\text{Ba}}^{(x)} \rangle$

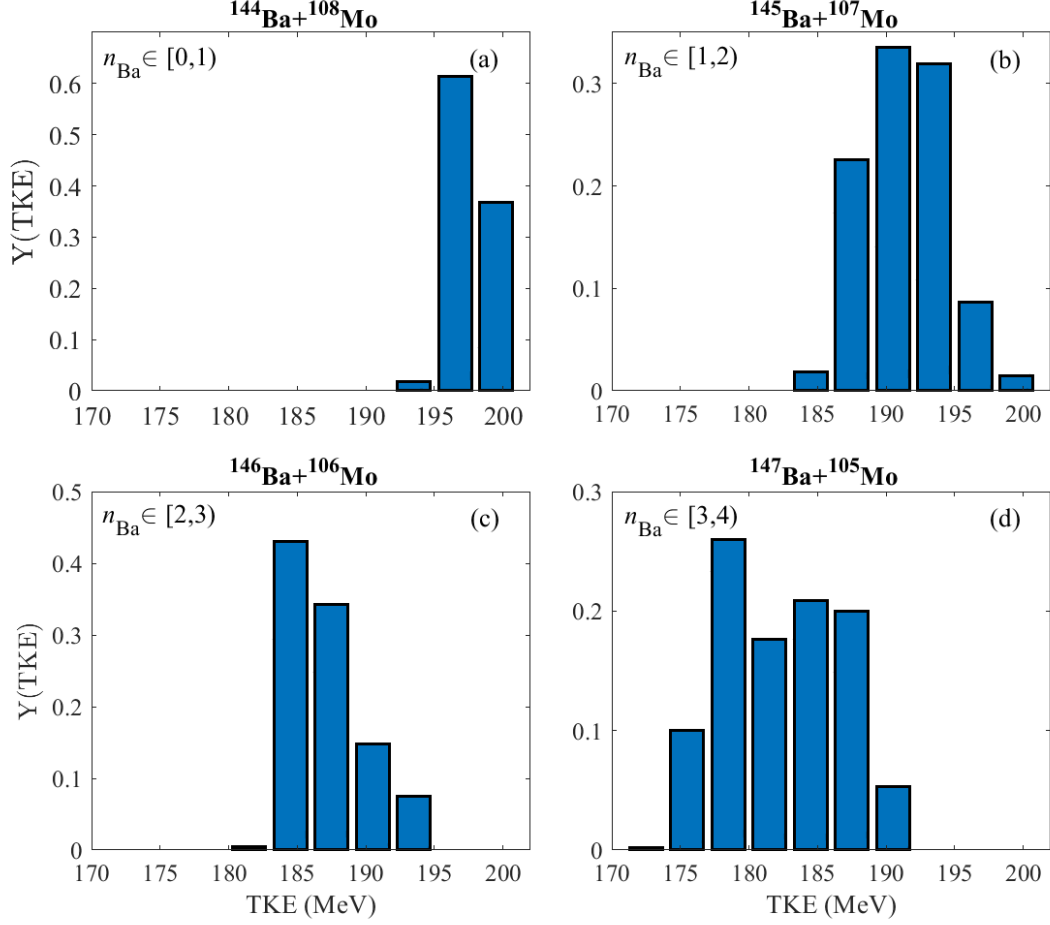


FIG. 4: The calculated total kinetic energy distributions for the decay from various scission configurations leading to post-scission fragment ^{144}Ba . Each TKE distribution presented here is normalized to unity for better visibility.

and $\langle I_0^{(x)} \rangle$ are given. To the left side of each level the excitation energies E_x are indicated. As seen, the average angular momenta grows with increasing E_x . However, the first excited state lies at 1.78 MeV. If we estimate the temperature T of DNS using the Eq. (5), we obtain $T = 0.44$ MeV which is sufficiently smaller than E_x . Therefore, only the ground-state contributes significantly to the generation of angular momenta of fragments. The same holds true for other DNS studied (see Table. II for comparison between E_1 and T).

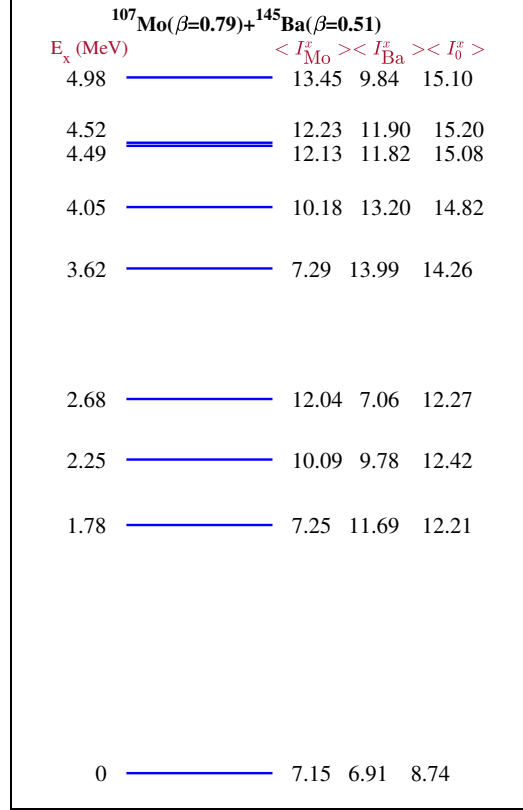


FIG. 5: The spectrum of angular motion in DNS: $^{107}\text{Mo}(\beta_{\text{Mo}} = 0.79)+^{145}\text{Ba}(\beta_{\text{Ba}} = 0.51)$ is shown. The excited states are marked by the lines, with average angular momenta $\langle I_{\text{Mo}} \rangle$, $\langle I_{\text{Ba}} \rangle$ and $\langle I_0 \rangle$ listed to the right and excitation energies E_x to the left of each level.

D. Average angular momenta of primary fission fragments

The calculated average angular momenta of Ba isotopes which lead to ^{144}Ba after neutron emission are shown in Fig. 6 (a). As seen, the average angular momenta $\langle I_{\text{Ba}} \rangle$ versus TKE are almost constant for each scission configuration. As mentioned above, since the number of neutrons emitted from Ba isotopes is fixed, the deformation of Ba changes only slightly while variation in TKE is achieved due to change of deformation of the corresponding Mo isotopes. As shown in Ref. [20], the average angular momenta of Mo and Ba pairs are uncorrelated and the average angular momenta of Ba isotopes stay almost constant within the available TKE range. Additionally, angular momentum increase due to excitation of higher states of angular motions is almost negligible because the excitation energies of the considered configurations are rather small (see Fig. 6 (b)).

While for each scission configuration, the average angular momentum of the corresponding

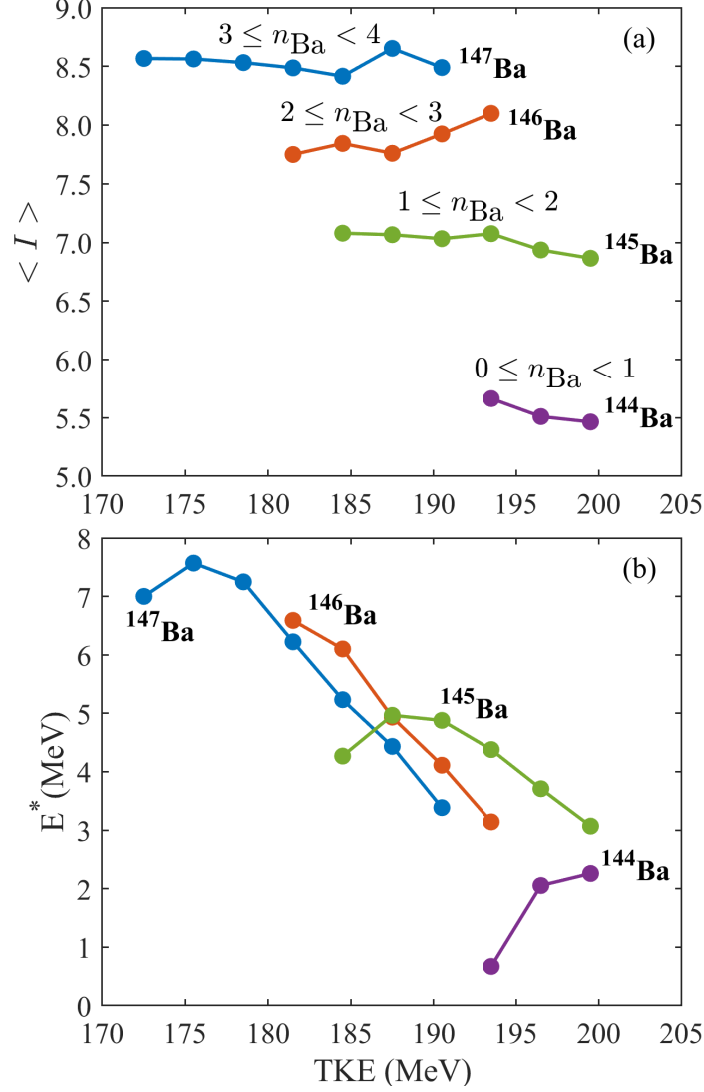


FIG. 6: The calculated average angular momenta (panel a) and excitation energies (panel b) of Ba isotopes in scission configurations leading to ^{144}Ba after n_{Ba} neutron emissions, plotted against total kinetic energy TKE.

Ba isotope is practically constant, it differs from one scission configuration to another. Having maximum value ($\langle I_{\text{Ba}} \rangle \approx 8.65$) for the DNS: $^{147}\text{Ba} + ^{105}\text{Mo}$, it decreases up to $\langle I_{\text{Ba}} \rangle \approx 5.46$ for DNS: $^{144}\text{Ba} + ^{108}\text{Mo}$. The reason for this is clearly seen from Fig. 3 where decay probabilities for various DNS configurations leading to post-scission ^{144}Ba are displayed in the plane $(\beta_{\text{Ba}}, \beta_{\text{Mo}})$. The decay probability is localized in different regions of deformation of Ba fragment. For ^{144}Ba pre-scission fragment, decay occurs mainly from $\beta_{\text{Ba}} \sim 0.2$, for ^{145}Ba – $\beta_{\text{Ba}} \sim 0.4$, for ^{146}Ba – $\beta_{\text{Ba}} \sim 0.7$, and for ^{147}Ba – $\beta_{\text{Ba}} \sim 0.92$. As explained in details in

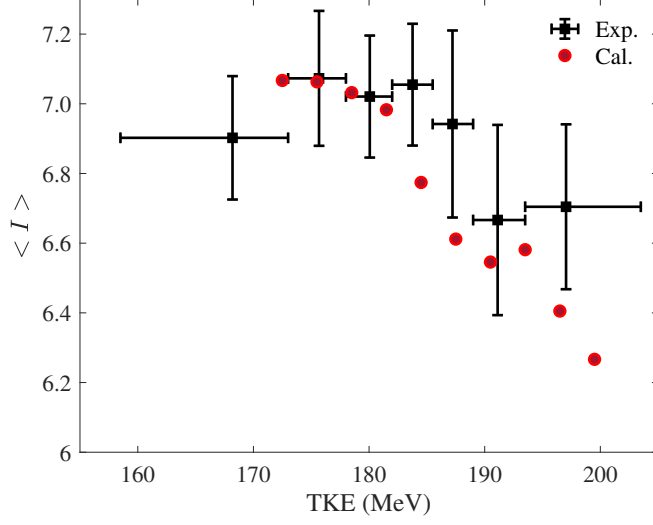


FIG. 7: Average angular momentum $\langle I \rangle$ of post-scission ^{144}Ba (red circles) as a function of total kinetic energy (TKE), compared with experimental data from Ref. [1] (black squares).

Ref. [20], the average angular momentum of a DNS fragment increases with its deformation.

E. Average angular momenta of ^{144}Ba and accompanying Mo fission fragments versus TKE

If several DNS configurations contribute to the average angular momenta within a given TKE interval, we average them out using their corresponding decay probabilities presented in Table. II. Following experimental observations and discussion in Refs. [1], neutrons are assumed to be emitted as s -waves. Therefore, each neutron is assumed to carry away $\hbar/2$ unit of angular momentum. Hence, to calculate average angular momentum of post-scission ^{144}Ba , in addition to averaging we should take into account the different number of emitted neutrons from the pre-scission Ba fragment:

$$\begin{aligned} \langle I_A \rangle &= \langle I(^A\text{Ba}) \rangle - (A - 144)/2, \\ \langle I \rangle &= \sum_{A=144,145,146,147} P_d(^A\text{Ba}) \langle I_A \rangle / \sum_{A=144,145,146,147} P_d(^A\text{Ba}). \end{aligned} \quad (37)$$

The result of calculations for average angular momentum $\langle I \rangle$ of post-scission ^{144}Ba versus TKE is presented in Fig. 7, together with the experimental data from Ref. [1]. The absolute value of average angular momentum is in a good agreement with the experimental data and

its trend is well reproduced by the calculations. The change of angular momentum in the range of TKE from 173 MeV up to 200 MeV is limited to $0.8 \hbar$. In the TKE range of 170-180 MeV the $\langle I \rangle$ values stay constant. This is related to the fact that in this range of TKE only one scission configuration $^{147}\text{Ba}+^{105}\text{Mo}$ contributes. The contributions of the DNS $^{146}\text{Ba}+^{106}\text{Mo}$ starting from TKE=181.5 MeV, and of the DNS $^{145}\text{Ba}+^{107}\text{Mo}$ starting from TKE=184.5 MeV lead to gradual but slight decrease of angular momentum with increasing TKE. The local minimum is achieved at TKE=190.5 MeV where the contribution of the DNS $^{147}\text{Ba}+^{105}\text{Mo}$ ends. Further increase of TKE leads to slight increase in average angular momentum because of the contribution of the DNS $^{146}\text{Ba}+^{106}\text{Mo}$. This up-bending at TKE ≈ 190 MeV is also seen in the experimental data. Finally, when the contribution of DNS $^{146}\text{Ba}+^{106}\text{Mo}$ comes to a halt at TKE=193.5 MeV, the decrease of $\langle I \rangle$ continues. The decrease of angular momentum in the region of TKE > 193.5 is related to the contribution of two DNS $^{145}\text{Ba}+^{107}\text{Mo}$ and $^{144}\text{Ba}+^{108}\text{Mo}$. Note that the relative yield of the later DNS configuration is at least one order of magnitude smaller (see Table II) which possibly makes it hard to observe experimentally the events related to the decay of this system. If this DNS is excluded from our calculations the dependence of angular momentum on TKE gets even weaker.

To summarize, the model presented is capable to explain the weak dependence of average angular momentum on TKE for the post-scission isotope ^{144}Ba . There are three reasons for this weak dependence. Firstly, the change in TKE at a constraint of certain number of emitted neutrons from Ba isotope mainly occurs due to the variation of deformation of the corresponding Mo fragment. Secondly, the most of energy available for neutron emission is stored as deformation energy while the excitation energy at scission is rather small and the excitation of higher-lying states of collective angular motions is strongly hindered. Finally, the larger number of emitted neutrons leads to the decrease of angular momentum of post-scission fragment.

The observation that the change of TKE is mainly due to variation of deformation of Mo fragments gives an interesting possibility to check the validity of the model proposed. If in coincidence with measurement of ^{144}Ba the angular momentum of all Mo isotopes is measured, its trend versus TKE is expected to be different from that for ^{144}Ba .

In Fig. 8, we present the average angular momentum of pre-scission ^{105}Mo as a function of β_{Mo} . The deformation of Ba is kept at $\beta_{\text{Ba}} = 0.92$ which corresponds to the maximum decay

probability of the DNS $^{147}\text{Ba}+^{105}\text{Mo}$ (see Fig.3). We see that average angular momentum of the pre-scission ^{105}Mo fragment exhibits a rapid increase at small deformations. This trend eventually ends up with an asymptotic at larger deformations. After accounting for the angular momentum carried away by the emitted neutrons, which tend to increase at larger deformations, we anticipate a maximum average angular momentum, $\langle I \rangle$, for Mo at intermediate deformations.

The angular momenta of pre-scission Mo isotopes are shown in Fig. 9 (a). As seen, the angular momenta decrease gradually with increasing TKE (decreasing Mo deformation). After accounting for the angular momenta carried away by emitted neutrons the decline of angular momentum with TKE is generally reduced (see Fig. 9 (b)). It is specially interesting in the case of ^{105}Mo which exhibits a maximum at $\text{TKE} \approx 175$ MeV which appears due to the competition between increase of angular momentum and the number of emitted neutrons with deformation. Summing up the contribution of different DNS at scission we obtain the dashed black line which corresponds to average angular momentum of Mo isotopes versus TKE measured in coincidence with ^{144}Ba .

It is seen that angular momentum of Mo varies in a wider range ($\approx 1\hbar$) than that of ^{144}Ba . While the angular momentum of ^{144}Ba stays almost constant and then slightly decreases with increasing TKE, the trend of Mo average angular momentum is opposite. Finally, in the region of low TKE, the angular momentum of Mo isotopes shows a local maximum at $\text{TKE} \approx 175$ MeV. Therefore, it seems interesting to investigate the average angular momentum of all Mo isotopes measured in coincidence with ^{144}Ba .

IV. CONCLUSIONS

We propose a model to describe the evolution of a fissioning nucleus after tunneling through the fission barrier as a random walk among various scission configurations. The nucleus is represented as a superposition of various DNS. The competition between DNS decay and its evolution in mass/charge asymmetry and fragments deformations leads to the formation of primary fission fragment distribution. The relative probabilities of initially formed DNS and the transition rates between them are determined by their level densities. The collective states associated with angular motion in the DNS are treated quantum-mechanically, as in Ref. [20], and are included in the calculations. The model is applied

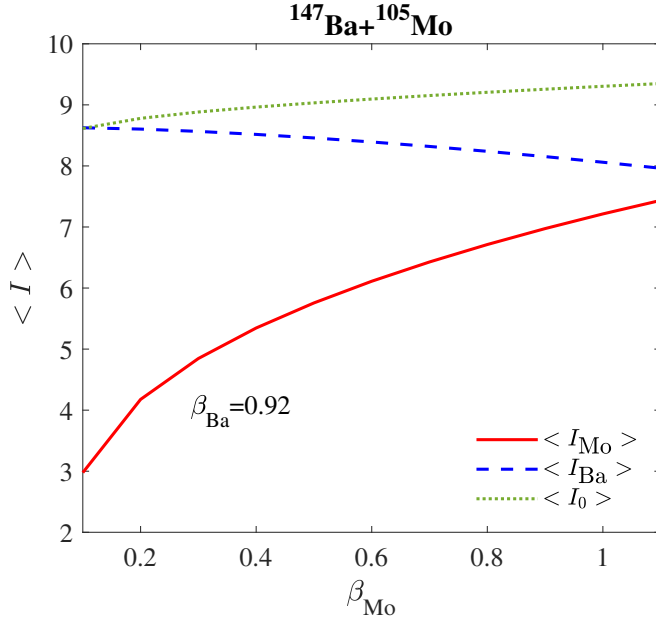


FIG. 8: Calculated average angular momenta of pre-scission ^{105}Mo ($\langle I_{\text{Mo}} \rangle$), ^{147}Ba ($\langle I_{\text{Ba}} \rangle$), and the DNS as a whole ($\langle I_0 \rangle$) versus β_{Mo} . The deformation of ^{147}Ba is fixed at $\beta_{\text{Ba}} = 0.92$, corresponding to the maximum decay probability for the DNS: $^{147}\text{Ba} + ^{105}\text{Mo}$ (see Fig. 3).

to determine key fission observables in the SF of ^{252}Cf . The calculated mass, TKE, and neutron multiplicity distributions agree well with experimental data. Further, for different values of TKE, we identify the DNS configurations yielding the post-scission fragment ^{144}Ba after neutron emission. For these configurations, the average angular momenta of the DNS fragments are computed. By summing the contributions of the selected DNS and assuming that neutrons are emitted as s -waves, we determine the dependence of the post-scission ^{144}Ba angular momentum on TKE. The results well describe the recent experimental data from Ref. [1], confirming the weak correlation between fission fragment angular momenta and TKE. Additionally, we present the average angular momentum dependence for Mo fission fragments measured in coincidence with ^{144}Ba .

Acknowledgments

This work was supported by a grant №25-42-00018 from the Russian Science Foundation [55]. We thank the authors of Ref. [1] for kindly providing the experimental data. A. Rahmatinejad gratefully acknowledges the generous support of F. Gorji and H. Tofightehrani-

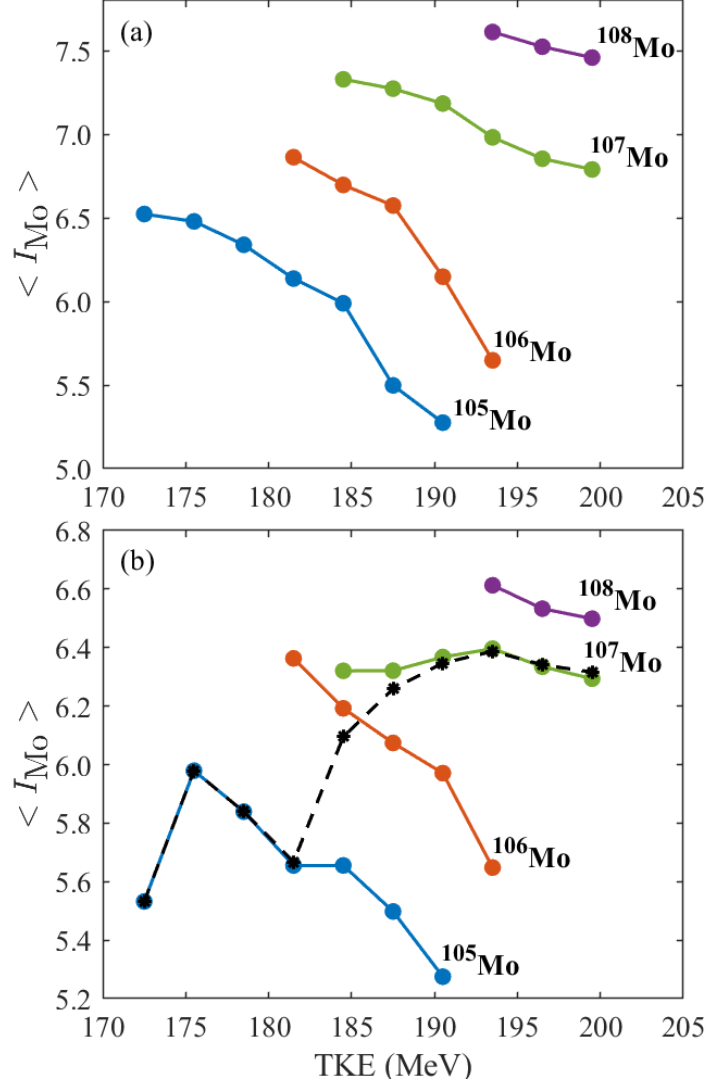


FIG. 9: Calculated average angular momentum of pre-scission (panel a) and post-scission (panel b) Mo isotopes in the DNS configurations leading to ^{144}Ba after neutron emission versus the total kinetic energy TKE. The dashed black line represents the summed contribution of various DNS configurations at scission, corresponding to the average angular momentum of Mo isotopes measured in coincidence with ^{144}Ba versus TKE.

monfared during the course of this research.

-
- [1] N. P. Giha *et al.*, Phys. Rev. C **111**, 014605 (2025).
 - [2] A. Göök, F.-J. Hambsch, and M. Vidali, Phys. Rev. C **90**, 064611 (2014).

- [3] J. B. Wilhelmy, E. Cheifetz, R. C. Jared, S. G. Thompson, H. R. Bowman, and J. O. Rasmussen, Phys. Rev. C **5**, 2041 (1972).
- [4] F. Pleasonton, R. L. Ferguson, and H. W. Schmitt, Phys. Rev. C **6**, 1023 (1972).
- [5] A. Wolf and E. Cheifetz, Phys. Rev. C **13**, 1952 (1976).
- [6] G. M. Ter-Akopian *et al.*, Phys. Rev. Lett. **73**, 1477, (1994).
- [7] J. R. Nix and W. J. Swiatecki, Nucl. Phys. **71**, 1 (1965).
- [8] J. O. Rasmussen, W. Nörenberg, and H. J. Mang, Nucl. Phys. A **136**, 465 (1969).
- [9] M. Zielinska-Pfabé and K. Dietrich, Phys. Lett. B **49**, 123 (1974).
- [10] S.G. Kadmsky, D.E. Lubashevsky, and L.V. Titova, Bull. Russ. Acad Sci.: Phys., **79**, 879 (2015).
- [11] J. Randrup and R. Vogt, Phys. Rev. Lett. **127**, 062502 (2021).
- [12] J. Randrup, Phys. Rev. C **106**, L051601 (2022).
- [13] G. F. Bertsch, T. Kawano, and L. M. Robledo, Phys. Rev. C **99**, 034603 (2019).
- [14] P. Marević, N. Schunck, J. Randrup, and R. Vogt, Phys. Rev. C **104**, L021601 (2021).
- [15] A. Bulgac, I. Abdurrahman, K. Godbey, I. Stetcu, Phys. Rev. Lett. **128**, 022501 (2022).
- [16] T. M. Shneidman, G. G. Adamian, N. V. Antonenko, S. P. Ivanova, R. V. Jolos, and W. Scheid, Phys. Rev. C **65**, 064302 (2003).
- [17] T. Dössing, S. Åberg, M. Albertsson, B. G. Carlsson, and J. Randrup, Phys. Rev. C **109**, 034615 (2024).
- [18] G. Scamps and G. Bertsch, Phys. Rev. C **108**, 034616 (2023).
- [19] J. N. Wilson *et al.*, Nature **590**, 566 (2021).
- [20] T. M. Shneidman, A. Rahmatinejad, G. G. Adamian and N. V. Antonenko, arXiv:2409.10114 [nucl-th] (2024).
- [21] A. Rahmatinejad, A. V. Andreev, A. N. Bezbakh, A. V. Isaev, R. S. Mukhin and T. M. Shneidman, Int. J. Mod. Phys. E **33**, 2441018 (2024).
- [22] A. Bulgac, S. Jin, K. J. Roche, N. Schunck, I. Stetcu, Phys. Rev. C **100**, 034615 (2019).
- [23] G. G. Adamian et al., Int. Jour. Mod. Phys. E **5**, 191 (1996).
- [24] W. D. Myers and W. J. Swiatecki, Nucl. Phys. **81**, 1 (1966).
- [25] J. Maruhn and W. Greiner, Z. Phys. A **251**, 431 (1972).
- [26] S. G. Nilsson, and I. Ragnarsson, *Shapes and Shells in Nuclear Structure*, Cambridge University Press, 1995.

- [27] A. N. Kuzmina, G. G. Adamian, N. V. Antonenko, W. Scheid, Phys. Rev. C **85**, 014319 (2012).
- [28] P. Möller, A. J. Sierk, T. Ichikawa, H. Sagawa, At. Data Nucl. Data Tables **109**, 1 (2016).
- [29] A. Bezbakh et al., Eur. Phys. J. A **52**, 353 (2015).
- [30] P. Dekowski, W. Grochulski, A. Marinkowski, K. Siwek, and Z. Wilhelmi, Nucl. Phys. A **110**, 129 (1968).
- [31] G. D. Adeev and P. A. Cherdantsev, Yad. Fiz. **21**, 491 (1975).
- [32] A. N. Behkami and J. R. Huizenga, Nucl. Phys. A **217**, 78 (1973).
- [33] A. Rahmatinejad, T. M. Shneidman, N. V. Antonenko, A. N. Bezbakh, G. G. Adamian, and L. A. Malov, Phys. Rev. C **101**, 054315 (2020).
- [34] A. Rahmatinejad, A. N. Bezbakh, T. M. Shneidman, G. Adamian, N. V. Antonenko, P. Jachimowicz, and M. Kowal, Phys. Rev. C **103**, 034309 (2021).
- [35] A. Rahmatinejad, T. M. Shneidman, G. Adamian, N. V. Antonenko, P. Jachimowicz, and M. Kowal, Phys. Rev. C **105**, 044328 (2022).
- [36] A. Rahmatinejad, T. M. Shneidman, G. G. Adamian, N. V. Antonenko, P. Jachimowicz, M. Kowal, Eur. Phys. J. A **60**, 214 (2024).
- [37] G. Maino, A. Mengoni, and A. Ventura, Phys. Rev. C **42**, 988 (1990).
- [38] L.G. Moretto and J.S. Sventek, Phys. Lett. B **58**, 26 (1975).
- [39] G.G. Adamyan, A.K. Nasirov, N.V. Antonenko, R.V. Jolos, Fiz. Elem. Chastits At.Yadra **25**, 1379 (1994).
- [40] T. M. Shneidman, G. G. Adamian, N. V. Antonenko, S. P. Ivanova, W. Scheid, Nucl. Phys. A **671**, 119 (2000).
- [41] W. Nazarewicz and J. Dobaczewski, Phys. Rev. Lett. **68**, 154 (1992).
- [42] S. Ćwiok, W. Nazarewicz, J. X. Saladin, W. Płóciennik, and A. Johnson, Phys. Lett. B **322**, 304 (1994).
- [43] S. Åberg and L. O. Jonsson, Z. für Physik A **349**, 205 (1994).
- [44] A. B. Migdal, *Theory of Finite Fermi Systems and Applications to Atomic Nuclei*, (Wiley, New York, 1967).
- [45] T. M. Shneidman, G. G. Adamian, N. V. Antonenko, R. V. Jolos, and Shan-Gui Zhou, Phys. Rev. C **92**, 034302 (2015).
- [46] D. A. Varshalovich, A. N. Moskalev, and V. K. Khersonskii, *Quantum theory of angular momentum*, (World Scientific, Singapore, 1988).

- [47] A. Rahmatinejad, T. M. Shneidman, G. G. Adamian, N. V. Antonenko, P. Jachimowicz, M. Kowal, Phys. Lett. B **844**, 138099 (2023).
- [48] R. S. Mukhin *et al.*, Eur. Phys. J. A **60**, 11 (2024).
- [49] R. S. Mukhin *et al.*, Chinese Phys. C **48**, 064002 (2024).
- [50] A.V. Isaev *et al.*, Phys. Lett. B **843**, 138008 (2023).
- [51] G. M. Ter-Akopian *et al.*, Phys. Rev. C **55**, 1146 (1997).
- [52] P. David, J. Debrus, F. Lobke, H. Mommsen, and R. Schoenmackers, Phys. Lett. **B** 60, 445 (1976).
- [53] N. E. Holden and M. S. Zucker, Radiation Effects **96**, 289 (1986).
- [54] A. S. Vorobyev *et al.*, AIP Conf. Proc. **769**, 613 (2005).
- [55] <https://rscf.ru/project/25-42-00018/>

TABLE II: The average deformations for each TKE bin together with the corresponding TKE values at the center of bins, decay probabilities and temperatures at the scission point for the chosen DNS.

$^{105}\text{Mo}+^{147}\text{Ba}$								
β_{Mo}	β_{Ba}	Yield	TKE (MeV)	T (MeV)	$\langle I_{\text{Mo}} \rangle \hbar$	$\langle I_{\text{Ba}} \rangle \hbar$	$\langle I_0 \rangle \hbar$	E_1 (MeV)
0.73	1.01	5.97×10^{-7}	172.50	0.53	6.52	8.57	9.37	2.14
0.67	0.96	3.02×10^{-5}	175.50	0.56	6.48	8.56	9.39	2.10
0.62	0.94	7.84×10^{-5}	178.50	0.54	6.34	8.53	9.32	2.05
0.57	0.92	5.33×10^{-5}	181.50	0.50	6.14	8.49	9.21	1.98
0.53	0.89	6.31×10^{-5}	184.50	0.45	5.99	8.42	9.11	1.98
0.40	0.91	6.02×10^{-5}	187.50	0.43	5.50	8.65	9.04	1.67
0.36	0.89	1.60×10^{-5}	190.50	0.37	5.28	8.49	8.95	1.59
$^{106}\text{Mo}+^{146}\text{Ba}$								
0.76	0.73	9.56×10^{-7}	181.50	0.44	6.86	7.75	9.02	2.14
0.70	0.74	9.78×10^{-5}	184.50	0.44	6.70	7.84	9.02	2.20
0.65	0.70	7.77×10^{-5}	187.50	0.39	6.57	7.76	8.92	2.19
0.53	0.73	3.36×10^{-5}	190.50	0.36	6.15	7.93	8.85	2.09
0.41	0.77	1.71×10^{-5}	193.50	0.33	5.65	8.10	8.80	1.81
$^{107}\text{Mo}+^{145}\text{Ba}$								
0.87	0.55	8.08×10^{-5}	184.50	0.40	7.33	7.08	8.92	1.79
0.83	0.53	9.66×10^{-4}	187.50	0.43	7.27	7.07	8.90	1.78
0.79	0.51	1.44×10^{-3}	190.50	0.43	7.18	7.03	8.84	1.78
0.71	0.50	1.37×10^{-3}	193.50	0.40	6.98	7.08	8.77	1.82
0.67	0.47	3.71×10^{-4}	196.50	0.37	6.85	6.94	8.63	1.81
0.63	0.44	6.27×10^{-5}	199.50	0.34	6.79	6.87	8.57	1.77
$^{108}\text{Mo}+^{144}\text{Ba}$								
0.91	0.29	3.86×10^{-7}	193.50	0.14	7.61	5.66	8.50	1.27
0.86	0.24	1.28×10^{-5}	196.50	0.28	7.52	5.51	8.40	1.19
0.83	0.23	7.68×10^{-6}	199.50	0.28	7.46	5.46	8.34	1.18